COLLISIONS OF CO$_2$ ICE GRAINS IN PLANET FORMATION

GRZEGORZ MUSIOLIK, JENS TEISER, TIM JANKOWSKI, AND GERHARD WURM
Fakultät für Physik, Universität Duisburg-Essen, Lotharstr. 1, D-47048 Duisburg, Germany; gregor.musiolik@uni-due.de

ABSTRACT

In protoplanetary disks, CO$_2$ is solid ice beyond its snow line at $\sim$10 AU. Due to its high abundance, it contributes heavily to the collisional evolution in this region of the disk. For the first time, we carried out laboratory collision experiments with CO$_2$ ice particles and a CO$_2$-covered wall at a temperature of 80 K. Collision velocities varied between 0 and 2.5 m s^{-1}. Particle sizes were on the order of $\sim$ 100 μm. We find a threshold velocity between the sticking and the bouncing regime at 0.04 m s^{-1}. Particles with greater velocities, but below 1 m s^{-1}, bounce off the wall. For yet greater velocities, fragmentation occurs. We give analytical models for the coefficients of restitution and fragmentation strength consistent with the experimental data. Set in context, our data show that CO$_2$ ice and silicate dust resemble each other in the collisional behavior. Compared to water ice, the sticking velocity is an order of magnitude smaller. One immediate consequence as an example is that water-ice particles mantled by CO$_2$ ice lose any "sticking advantage." In this case, preferential planetesimal growth attributed to the sticking properties of water ice will be limited to the region between the H$_2$O ice line and the CO$_2$ ice line.

Key words: planets and satellites: formation – protoplanetary disks

1. INTRODUCTION

The role of silicate dust and water ice in planetesimal formation by collisional growth has been studied for many years (Dominik et al. 2007; Blum & Wurm 2008; Johansen et al. 2014). The role of CO$_2$ ice and CO ice has not been touched upon yet in the framework of collisional evolution, although carbon oxides are highly abundant. For comet Churyumov–Gerasimenko, *Rosetta* recently found significant CO$_2$ gas fractions in the coma composition (Hässig et al. 2015). Pontoppidan et al. (2014) and Öberg et al. (2011) estimate the number ratios of H$_2$O:CO$_2$:CO and give values of 100:38:31 in cloud core environments and 100:13:13 toward protostars.

In the general scheme of planetesimal formation, the ices of these volatiles play a role beyond their snow lines. Ali-Dib et al. (2014) suggest that the formation of Uranus and Neptune might be tight to the CO ice line. For TW Hya, observations by ALMA imply the existence of a CO ice line at $\sim$30 AU (Qi et al. 2013). Further inward though is the CO$_2$ ice line. Its position can be calculated using the sublimation pressure curve and a disk model. We fitted the experimental sublimation pressure data from Bryson et al. (1974) with a modified sublimation pressure curve from Span & Wagner (1996), leading to

$$\ln\left(\frac{p_{sub}}{p_c}\right) = \frac{T_c}{T}\left[k_1\left(1 - \frac{T}{T_c}\right)^{l_1} + k_2\left(1 - \frac{T}{T_c}\right)^{l_2}\right] \quad (1)$$

with $T_c = 216.592$ K, $p_c = 0.51795$ MPa, $k_1 = -12.3081445$, $k_2 = -5.3061778$, $l_1 = 0.8472$, $l_2 = 3.47023$. Using the minimum mass solar nebula (MMSN) disk properties by Hayashi et al. (1985) and setting $p_{sub} = p_{disk}$, the CO$_2$ snow line can be calculated to be at 9.3 AU. With the same method, the H$_2$O snow line is calculated to be at 2 AU. Using different models and calculation methods, the CO$_2$ and H$_2$O snow lines might shift, but, in general, the values are consistent with those from other authors, like Öberg et al. (2011), for example.

Essentially no data exist to date on the collisional behavior of CO$_2$ ice grains. We note that there are investigations related to CO$_2$ snow. These have applications on Earth in mind, e.g., Lin et al. (2014) explain an agglomeration mechanism of 100 μm sized CO$_2$ snow inside a tube and describe its dependency on jet flows with vortices. This cannot be applied to astrophysical environments directly, though. Quantitative experimental studies similar to those made for planetesimal formation with silicates (Wurm et al. 2005; Blum & Wurm 2008; Güttler et al. 2010; Teiser et al. 2011) or H$_2$O ice (Aumatell & Wurm 2011, 2014; Gundlach & Blum 2015) are missing so far.

In the context of planetesimal (or comet) formation, it is important to know threshold velocities between sticking and bouncing as a function of grain size for all relevant condensed species. It is also important to have an estimate of how much energy is dissipated in a bouncing collision. Last but not least, the onset and strength of fragmentation are also fundamental properties to know. Wettlaufer (2010), e.g., considers collisional fusion of ice, where dissipation might lead to local heating and sintering, which might be important at higher temperatures. Wurm et al. (2001) consider reaccretion of particles after a collision by gas drag. Currently, this is also detailed by T. Jankowski et al. (2015, in preparation), and the rebound speed would be important then.

It should be obvious, but we would like to stress that CO$_2$ and H$_2$O are quite different. Besides the general common feature of volatility that kind of labels both solid phases as ice, it is a priori not possible to equal the collisional behavior of CO$_2$- and H$_2$O-ice without considering the microphysics of collisional particle interaction. In contrast to H$_2$O, CO$_2$ molecules do not have any electrical dipole moment (Morrison & Hay 1979). This is important for cohesion and collisional sticking. As shown in this paper, the term ice is not a synonym for sticky. Therefore, a possible zoned setting of a protoplanetary disk might look like Figure 1. The idea underlying this picture is an onion-like grain structure. The most refractory material is in the center; the most volatile ice is on the surface. This picture can be found throughout the literature (Fayolle et al. 2011; Sirono 2013). As shown later, growth of particles
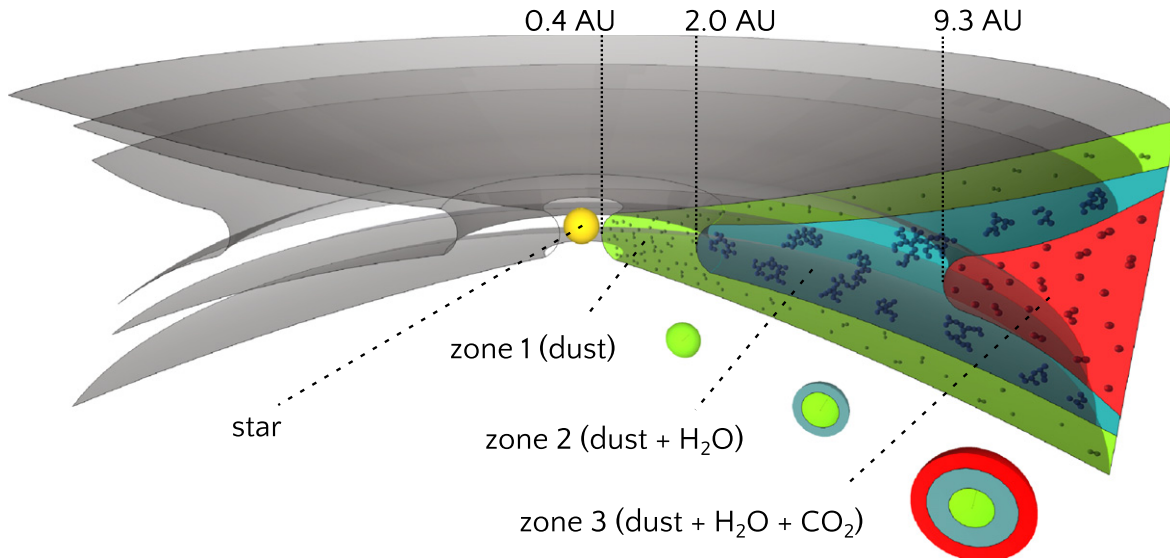
Figure 1. Initial setting of a protoplanetary disk. While in the first zone only silicate particles exist, in the second zone beyond the H_2O snow line the silicate particles might be covered by water ice. The CO_2 snow line indicates the beginning of the third zone, where silicate particles are coated with two layers: one inner H_2O layer and an outer CO_2 layer. Note that for better visualization the coatings are solid and colored, green: silicates; blue: H_2O; red: CO_2. While within the first, silicate-dominated zone as well as in the third, CO_2-dominated zone particles cannot grow quickly to larger sizes, H_2O coated particles in the second zone might grow to larger sizes more efficiently.

might preferably happen in zone 2, where H_2O ice dominates the collisional behavior.

In a complex scenario of sublimation and recondensation, especially in the vicinity of the different ice lines, the picture of layered grains might be somewhat simplified. However, it will readily show the potentially wide implications of the CO_2 collisional behavior. Mostly moderated by surface forces, the material of the outermost layer counts at least for major species like CO_2 that can build sufficient mantle thickness.

The composition of the mantle determines the range of velocities and particle masses/sizes for which hit-and-stick collisions occur as grains collide (Geretshauser et al. 2011). For silicates in the warm region (zone 1 in Figure 1), growth via collisions easily works to millimeter size. However, from this size on, particles tend to bounce off each other rather than stick together. This is known as the bouncing barrier (Zsom et al. 2010) and has also been shown to be a robust finding in experiments (Kelling et al. 2014). If large grains are introduced by some way collisional growth can still proceed (Wurm et al. 2005; Teiser & Wurm 2009; Windmark et al. 2012; Deckers & Teiser 2014). This is based on collisions with fragmentation where part of a smaller body is added to the larger one.

In the cooler regions of the disk (zone 2 in Figure 1), water ice is the next solid to dominate the collisional outcome. Due to the increased surface energy of the water ice with its polar molecules, bindings are much stronger and particles can grow larger. This has been seen in numerical simulations (Dominik & Tielens 1997; Wada et al. 2009) and laboratory experiments (Aumatell & Wurm 2014; Gundlach & Blum 2015). Okuzumi et al. (2012) even considered this to lead to very large planetesimal-size porous ice aggregates. Follow up work by Kataoka et al. (2013) also supports this view. In total, zone 2 seems very favorable for collisional planetesimal formation due to the properties of water ice.

We note that other concepts of planetesimal formation are also intensively studied currently. To span the gap from sub-meter particles to planetesimal gravito-turbulent concentration, concentration in baroclinic instabilities or streaming instabilities are considered to concentrate solids within the disk to a point of gravitational collapse (Chiang & Youdin 2010; Dittrich et al. 2013; Johansen et al. 2014). Both kinds of formation mechanisms—collisional growth and gravitational instabilities—might also go hand in hand. More efficient sticking might provide the necessary seeds of certain sizes for instabilities more easily (Johansen et al. 2014).

To date, also partly due to the increased mass reservoir of solids, giant-planet cores are most often supposed to be formed beyond the water snow line, and formation models are typically set in this regime (Pollack et al. 1996; Helled et al. 2014). Close-in giant planets are thought to be migrated there afterward (Kley & Nelson 2012; Baruteau et al. 2013; Dittkrist et al. 2014). In any case, the difference between zone 1 and zone 2 is evident with zone 2 being the one supposed to favor rapid formation of larger bodies.

Not considered so far is how far zone 2 extends. Further outward in a disk, other ice lines exist. As outlined above, CO_2 is very abundant. We consider it to be the next major ice line. In the picture of mantled grains, colliding grains beyond this line will no longer be dominated by water-ice properties. It is therefore important to know how the picture changes for CO_2 particles.

In this paper, we quantify collisional outcomes between $\sim 100\,\mu m$ sized CO_2 particles and a CO_2-covered wall at a temperature of $80\,K$ and ambient pressure of 0.5 mbar. The collision velocities reach from 0 to $2.5\,m\,s^{-1}$. We determine the impact velocity thresholds between sticking, bouncing, and fragmentation. Furthermore, we study the fragment size distribution when critical fragmentation occurs. We present an analytical model for fragmentation and restitution that describes the measured collisional behavior, which we finally put in context of planetesimal formation.
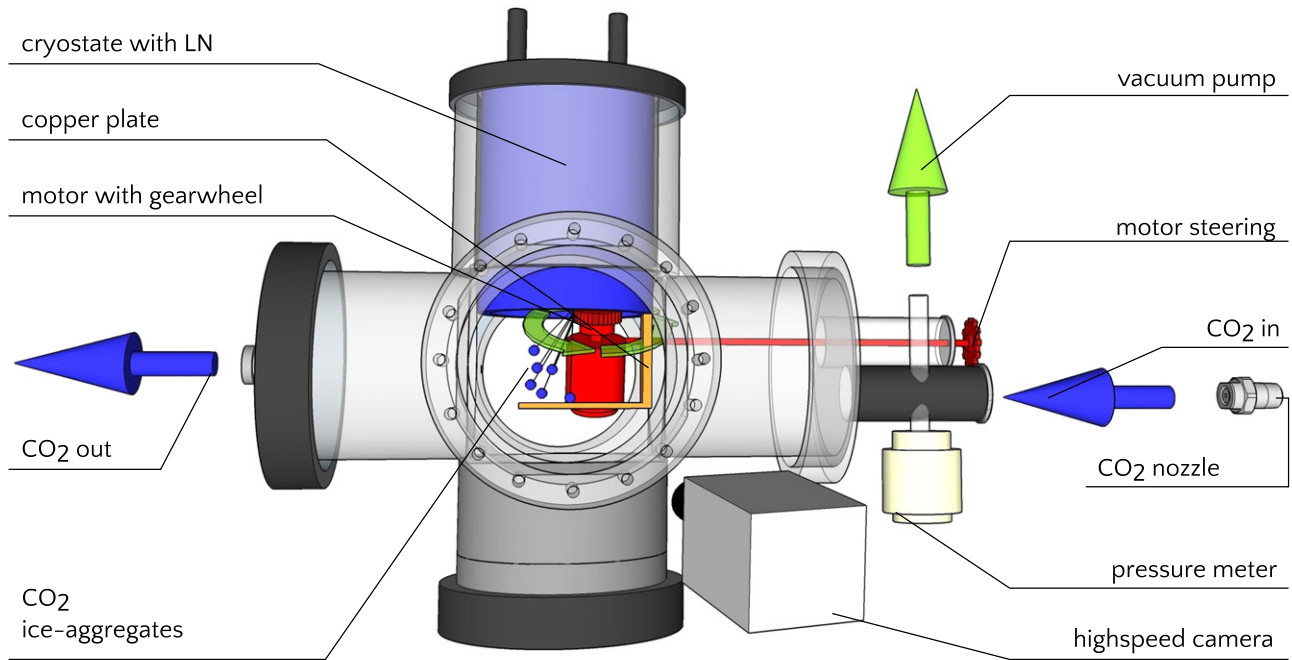
Figure 2. Experimental setup. Within a vacuum chamber, a liquid-nitrogen-cooled cryostat cools the top flange. The chamber is flooded with gaseous CO_2 which is deposited at the cryostat and a thermally coupled copper plate below the cryostate, forming an approximately 2 mm thick layer of solid CO_2. Using a cogwheel placed on a motor, ice aggregates can be beveled off the cryostat and the particles collide with the CO_2 layer at the copper plate.

2. EXPERIMENTAL SETUP

The setup of the experiment is shown in Figure 2. The experiment consists of a vacuum chamber, a liquid-nitrogen-cooled cryostat with a connected copper plate 15 cm below, a CO_2 injecting nozzle, and a motor with a cogwheel.

As a first step, the vacuum chamber is flooded with CO_2 gas. Since CO_2 gas is deposited on surfaces below 195 K for atmospheric pressures, a 2 mm thick, solid CO_2 ice layer grows on the walls of the cryostate and on the copper plate within several minutes. In a second step, the vacuum chamber is sealed and evacuated to an ambient pressure of 0.5 mbar. Using the motor with the gearwheel, which can be slided and rotated along the chamber from the outside, CO_2 ice can then be beveled off the cryostate and collide at speeds below 2.5 m s^{-1} with the CO_2 layer on the copper plane. Low-velocity collisions at $\sim$0.05 m s^{-1} can be observed due to rebound and gas–grain coupling of the aggregates. The collisions are imaged using a high-speed camera with a microscope lens recording at 1250 frames per second. The spatial resolution is limited to 10 μm. Sample images from the data set are shown in Figure 3.

In total, we performed around 20 experiments and evaluated 96 collision events therein.

3. RESULTS AND DISCUSSION

For further analysis, we consider the particles to be spheres with a density of 1560 kg m^{-3} (Mazzoldi et al. 2008). We take the radius of a sphere with the same cross section as the observed particle. Figure 4 shows the distribution of the particle radii used for this study.

Irregular grains might behave differently in individual collisions compared to spherical particles. Blum & Wurm (2000) and Poppe et al. (2000) suggest irregular grains of the same size to be slightly stickier. However, it is mostly the size that determines the threshold velocity for sticking. We
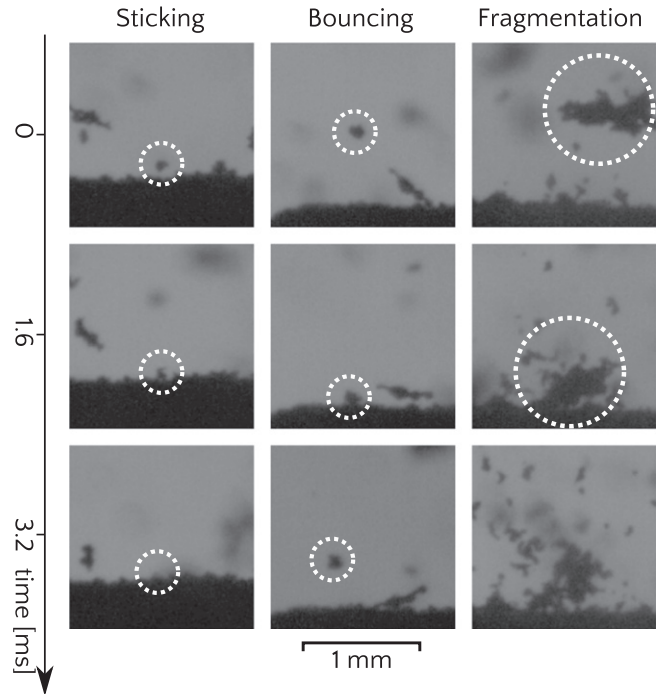

Figure 3. Sample images from the data set. CO_2 particles coming from the top are impinging the CO_2 ice layer at the bottom. Aggregates with surface equivalent radii greater than 500 μm were not studied. The examples show time sequences of the typical collisional outcomes observed: sticking, bouncing, fragmentation.

therefore consider our collisions to be representative of collisions of solid $\sim$100 μm CO_2 grains. This holds for the sticking and bouncing collisions. It should be noted that we could not unambiguously determine if the grains are monolithic or aggregates and the scaling to smaller sizes should only be considered as an order of magnitude estimate for these first
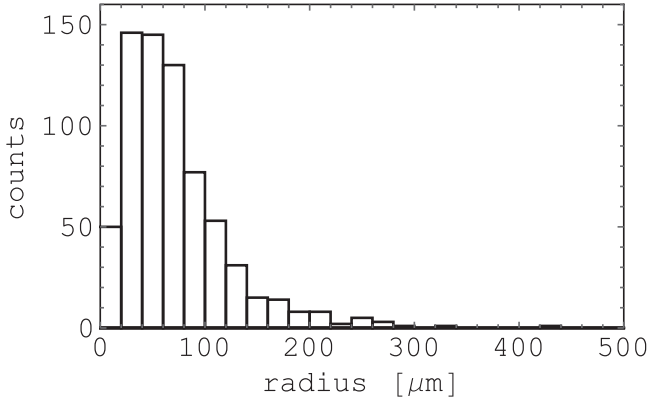
Figure 4. Size distribution of the CO_2 particles. 690 particles were analyzed. The average size is 71 μm. The bin size of 20 μm is chosen with respect to the spatial resolution of the optical system.
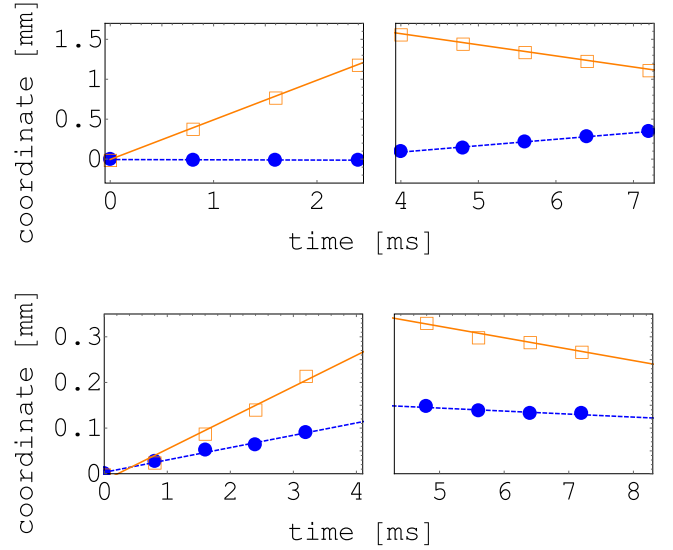

Figure 5. Two-dimensional motion of a bouncing particle with overplotted linear fit functions (circles for camera x-coordinate, squares for camera y-coordinate) before the collision (left) and after the collision (right). On top an example for higher velocities at about 1 m s^{-1} is shown. Below we give another example for velocities around 0.05 m s^{-1}.
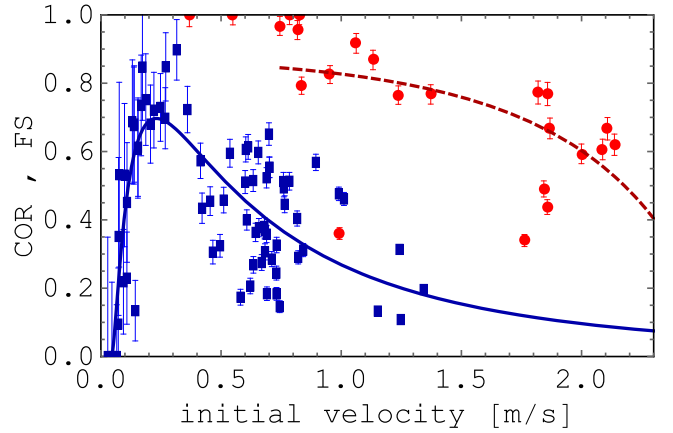

Figure 6. Coefficient of restitution (COR; blue squares) and the fragmentation strength (FS; red dots) of 96 CO_2 collisions. The data are fitted using the models for restitution (solid blue line; Equation (27)) and for fragmentation (dashed red line; Equation (16)).

experiments. For fragmentation at higher speeds, the outcome is influenced by the internal binding. If the larger grains (see Figure 3 right) are aggregates bound by surface forces, they fragment easily. If all connections are solid, they might not. Due to the formation mechanism of scraping grains from a solid surface, we do not know this a priori. However, the way the particles fragment into a large number of smaller units at low velocities indicates an aggregate structure. Comparing energies below supports this view that we produce grains of ~100 μm in diameter and aggregates thereof.

The collision behavior of dust depends mainly on the initial collision velocities and the masses of the grains and can be divided into several types (Güttler et al. 2010). 80% of all particles are in the size range between 40 and 120 μm. The average size of the particles is 71 μm. In terms of mass of individual grains and therefore energy (R^3), this is a variation in particle energy by a factor of about $120^3/40^3 = 27$. The collision velocity varies between 0.05 and 2.5 m s^{-1}, which in terms of energy (v^2) is a factor 2500, which is much larger than the energy variation by mass. Also, Figure 7 shows an extreme division for the coefficient of restitution for particles smaller and larger than 150 μm that show no difference. We therefore consider the velocity dependence of the coefficient of restitution to be representative of the average-size particles.

The CO_2 particles show the same well-known qualitative behavior as silicate particles. At low velocities, the CO_2 particles "hit & stick." If the speed is greater than a sticking velocity v_{stick}, the aggregates bounce off the surface in inelastic collisions. For these collisions, neither the surface is eroded nor do the particles fragment. Only at a greater velocity than v_{frag}, does fragmentation start. In our experiment, we were not able to see mass transfer during fragmenting collisions.

The motion of a particle can be approximated as linear in a time frame of ±5 ms around the collision, like Figure 5 shows exemplarily for two bouncing particles. By means of linear fits, we were able to determine the velocities of the particle before and after a collision $v_{i,x}$, $v_{i,y}$ and $v_{o,x}$, $v_{o,y}$ along the x (horizontal) and y (vertical) coordinates, respectively. We calculate the coefficient of restitution ϵ, which we define as the ratio

$$\epsilon(v_o, v_i) = \frac{v_o}{v_i} = \sqrt{v_{o,x}^2 + v_{o,y}^2} \big/ \sqrt{v_{i,x}^2 + v_{i,y}^2}. \qquad (2)$$

Moreover, we examined the fragmentation strength μ, which is the ratio of the largest fragment's mass m and the original aggregate mass m_0 after a fragmentation

$$\mu(m, m_0) = \frac{m}{m_0}. \qquad (3)$$

Figure 6 shows both quantities for all 96 observed collisions. The coefficient of restitution was evaluated for all grain sizes from Figure 4. As shown in Figure 7 the larger grains collide at greater velocities due to diminished gas drag. Where both size ranges are present, the coefficient of restitution shows no difference within the studied total range.

The coefficient of restitution peaks at an impact velocity of about 0.25 m s^{-1} and decreases continuously for increasing velocities. The data are fitted with the model functions for the coefficient of restitution (Equation (27)) and for the fragmentation strength (Equation (16)) as described in detail in the next section. We also fitted other restitution functions for ϵ, e.g., by
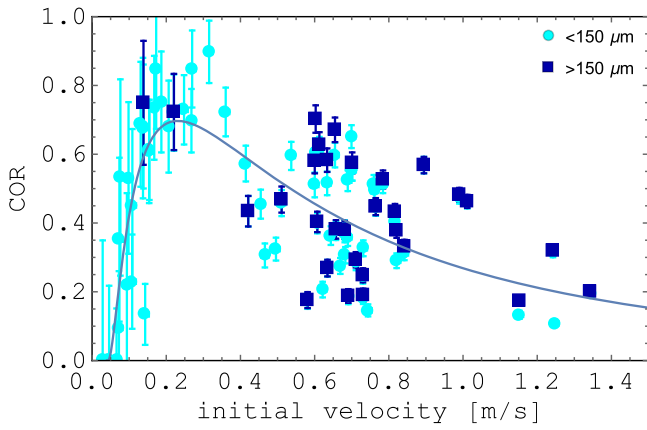
Figure 7. Coefficient of restitution for grains of different sizes. The separation is done with respect to the particles radii.

Figure 8. Comparison of different models for the coefficient of restitution.

Figure 9. Comparison between the fragmentation model in this work and Krijt & Kama (2014).

Higa et al. (1996, 1998), Andrews (1930), Borderies et al. (1984), Thornton & Ning (1998), Krijt et al. (2013), and a number of other models taken from Antonyuk et al. (2010). For none did we get as well matching fits. In fact, most of these models were originally used to describe restitution behavior in the inelastic regime and do not treat cohesion effects for velocities near the sticking limit. For adhesive models, Figure 8 shows the fitted curves for the coefficient of restitution.

For velocities around the sticking–bouncing transition, all of the shown models describe the behavior of the coefficient of restitution well. For high velocities in the fragmentation regime, Thornton & Ning (1998) and Krijt et al. (2013) predict a slope of $-1/4$, which is too flat. Compared to this, the empirical function from Higa et al. (1996, 1998) decreases too fast. The model that we present in this work contains the observed cohesive behavior at low velocities and strikes a balance between the other models shown in the fragmentation regime.

Regarding the fragmentation strength, Krijt & Kama (2014) investigated a fragmentation model recently. Their work mainly deals with the smallest fragment after collisions. Nevertheless, they give an expression for the largest spherical fragment from which we can derive a fragmentation strength, like Figure 9 shows. The curve fitted from Krijt & Kama (2014) fits as well to the data for the fragmentation events. However, it does not have a threshold for a transition between bouncing and fragmenting, which is clearly visible in the data. Beyond this model, we are not aware of any other analytical models for the fragmentation strength depending on the impact velocity, which we could compare to Equation (16).

We do see sticking at low collision velocities and a transition to bouncing. However, under gravity, sticking at very low speeds and bouncing with a very small coefficient of restitution cannot be disentangled. This spatial and temporal resolution limit is reached somewhat below $5\,\mathrm{cm\,s^{-1}}$ collision velocity. Therefore, to specify a single sticking velocity v_{stick}, we do not consider the sticking collisions but use our model fit function for the coefficient of restitution. We determine the velocity for $\epsilon = 0$ and find $v_{\mathrm{stick}} = (0.04 \pm 0.02)\,\mathrm{m\,s^{-1}}$. This sticking threshold is valid for particles with radii below $150\,\mu m$ only. As larger particles do also have larger velocities, no statement on their sticking velocity can be made, as Figure 7 shows. According to Dominik & Tielens (1997), the sticking velocity
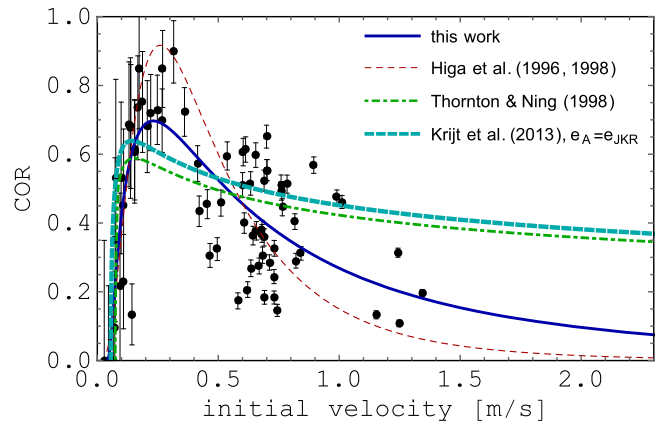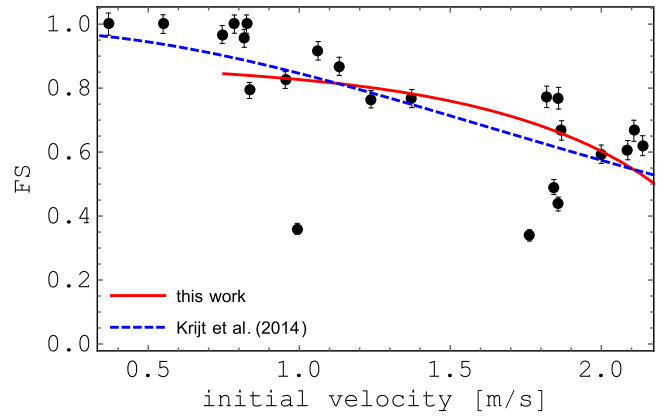
can be calculated as

$$v_{\mathrm{stick}} = \frac{1.07}{\rho^{1/2} E_{\mathrm{py}}^{1/3}} \cdot \frac{1}{R^{5/6}} \cdot \gamma^{5/6} \qquad (4)$$

with the surface energy γ, the reduced radius R, and the particle mass density ρ. The elastic properties enter via E_{py}, defined as $E_{\mathrm{py}} = E_{\mathrm{y}}/(2(1 - \nu_{\mathrm{p}}^2))$. Here, E_{y} is the Young's modulus and ν_{p} is the Poisson's ratio.

The first term (density, elasticity) is known for solid CO_2. The second term shows an almost inversely linear dependence on particle size. Even without knowing the third term (surface energy), the size dependence allows a comparison of our CO_2 data to data on silicate collisions and water-ice collisions. Experiments by Poppe et al. (2000) and Gundlach & Blum (2015) determined the sticking velocity of $\sim 1\,\mu m$ grains in collisions with walls. Poppe et al. (2000) found $v_{\mathrm{stick}} \approx 1.2\,\mathrm{m\,s^{-1}}$ for silica spheres with a $0.6\,\mu m$ radius colliding with a wall. For $1.5\,\mu m$ radius water ice spheres Gundlach & Blum (2015) found $v_{\mathrm{stick}} \approx 9.6\,\mathrm{m\,s^{-1}}$. They found roughly a factor of 10 increase in sticking velocity compared to silicates of similar size. Using the size dependence in Equation (4), we get $v_{\mathrm{stick}} \approx 1.2\,\mathrm{m\,s^{-1}}$ for $1.5\,\mu m$ radius CO_2 grains. This does not match the values for water ice but is rather close to the value for silica of a similar grain size. This is especially true considering that the CO_2 grains are not spherical as there seems to be a tendency that irregular grains have

somewhat higher sticking velocities in comparison to spheres (Poppe et al. 2000).

To allow an analytical treatment of CO_2 collisions for different parameters in the future, we extract the surface energy from our experiments as the single most important parameter. Using the longitudinal and transversal velocities $v_{lg} = 2900$ m s^{-1} and $v_{ts} = 1650$ m s^{-1} of sound in solid carbon dioxide for 80 K (Yamashita & Kato 1997), we can calculate Young's modulus $E_y = v_{lg}^2 \rho \approx 13.12$ GPa and the bulk modulus $G = v_{ts}^2 \rho \approx 4.25$ GPa. Finally, the Poisson ratio is given by $\nu_p = E/(2G) - 1 \approx 0.544$. With an average particle radius of 60 μm (only particles below 150 μm are relevant for sticking), this gives a surface energy of $\gamma = 0.17^{+0.26}_{-0.13}$ J m^{-3}. The error in γ results from the fit of the sticking velocity and the standard deviation from the size distribution. From the fragmentation model of Krijt & Kama (2014), we also get the surface energy as a fit parameter to $\gamma_K = (0.325 \pm 0.088)$ J m^{-2}, which is consistent with the value based on the sticking velocity. Compared to this, Wood (1999) estimates a surface energy for CO_2 between 0.08 and 0.097 J m^{-2}. Given the uncertainties of the particle contacts, one should keep in mind that the slightly larger value in our experiment are effective values for the specific given setting. Within these limits, the results are also consistent with the value by Wood (1999).

At $v_{frag} = (0.75 \pm 0.05)$ m s^{-1}, we find the onset of fragmentation as seen in Figure 3. The average kinetic energy at the onset of fragmentation is

$$E_{frag} = \frac{1}{2}\left(\frac{4\pi\rho r_m^3}{3}\right)v_{frag}^2 = (5.25 \pm 0.7) \cdot 10^{-10} \text{ J}. \quad (5)$$

According to Dominik & Tielens (1997), fragmentation for an aggregate occurs at an energy of

$$E_{frag} = 3nE_{br} \quad (6)$$

with E_{br} as energy to break contact that is 4.5 times the sticking energy E_{stick}, or

$$E_{frag}/E_{stick} = 13.5 \cdot n. \quad (7)$$

In our case, it is

$$E_{stick} = (1.38 \pm 1) \cdot 10^{-12} \text{ J} \quad (8)$$

and we get

$$E_{frag}/E_{stick} = 351 \quad (9)$$

for the onset of CO_2-aggregate fragmentation. This implies a number of 26 contacts, which is consistent with the fragment count of catastrophic collisions that we observed at higher impact speeds. In detail, the fragmentation energy depends on the size of an individual aggregate in a collision and its number of contacts. We cannot quantify this in a collision at the onset of fragmentation that is not completely catastrophic. Therefore, the considerations given before are more of a qualitative support of the aggregate nature of larger particles.

For very large aggregates, we analyzed the mass distribution $n(m)$ of the fragments of 12 collisions, where $n(m)dm$ means that n fragments are found in the mass range $[m; m + dm]$. We did not count the largest fragment and binned the data into 10 masses. The range of impact velocity varied between 0.6 and 2.2 m s^{-1}. The mass distribution is shown in Figure 10. This
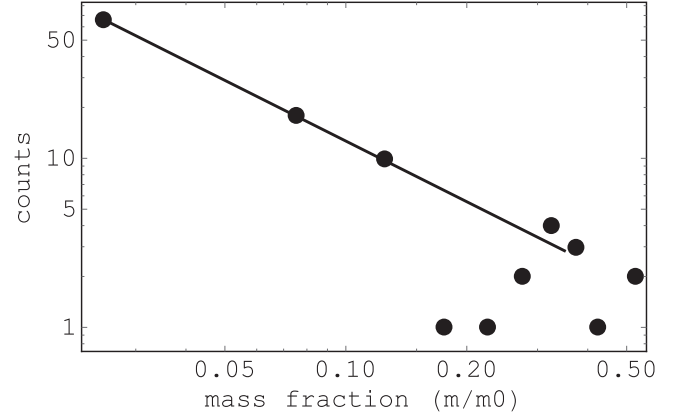

Figure 10. Number mass distribution of fragments after a catastrophic fragmentation. $m0$ is the mass of a whole aggregate before its fragmentation.

mass density function follows a power law

$$n \propto m^{-1.2\pm0.1}. \quad (10)$$

This falls into the range found for mass density distributions for silicate aggregate collisions where power laws with exponents between -1.07 and -1.36 are found (Güttler et al. 2010; Deckers & Teiser 2014). In this context, another way to characterize fragmentation is to estimate the critical fragmentation energy ($\mu = 0.5$). With $v_{crit} = (2.19 \pm 0.05)$ m s^{-1}, we get

$$E_{crit} = (4.47 \pm 0.2) \cdot 10^{-9} \text{ J}. \quad (11)$$

4. TWO NEW MODELS FOR FRAGMENTATION AND RESTITUTION

In this section, we develop our own models for the velocity dependence of fragmentation strength and coefficient of restitution.

4.1. Fragmentation Model

Our fragmentation model is based on an energy balance. The energy of the aggregate with mass M impacting with velocity v_i has to balance the kinetic energy of all fragments after the collision T_f, the energy to break the contacts and account for dissipated energy χ. We assume that each of the N fragments (subaggregates) stuck to the largest fragment with an energy of $\mathcal{V}$. The energy balance then reads

$$\frac{M}{2}v_i^2 = N\mathcal{V}\Theta(v_i - v_{frag}) + T_f + \chi. \quad (12)$$

Here, v_{frag} is the threshold velocity for fragmentation. The Heaviside function Θ implicates that disintegrations do not happen for $v_i < v_{frag}$. T_f is the total kinetic energy of all fragments after the collision. We assume that χ does not depend on v_i for $v_i > v_{frag}$. As seen before, the size distribution of the fragments follows a power law $n \propto a \cdot V^b$. Here, V is the fragment volume, and the constants a and b depend on the material properties (Güttler et al. 2010; Geretshauser et al. 2011). Therefore, we can express the fragment number in terms of volume and get

$$\frac{M}{2}v_i^2 = \mathcal{V}\Theta(v_i - v_{frag})\int_{V_{sf}}^{V_{frag}} dV\, a\, V^b + T_f + \chi. \quad (13)$$

with $V_{agg} = V_l + V_{frag}$, where V_{agg} is the volume of the total aggregate, V_l is the volume of the largest fragment, V_{sf} the volume of the smallest fragment, and V_{frag} is the volume of all fragments but without the largest. Integrated and solved for V_{frag}, this yields

$$V_{frag} = \left(\frac{(b+1)\left(\frac{M}{2}v_i^2 - T_f - \chi\right)}{a\mathcal{V}} + V_{sf}^{b+1} \right)^{1/(b+1)} \times \Theta(v_i - v_{frag}),$$ (14)

for $b < -1$.

The fragmentation strength $\mu(v_i)$ can then be described by

$$\mu(v_i) := \frac{V_l}{V_{agg}} = \frac{V_{agg} - V_{frag}}{V_{agg}}$$

$$= 1 - \frac{1}{V_{agg}}\left(\frac{(b+1)\left(\frac{M}{2}v_i^2 - T_f - \chi\right)}{a\mathcal{V}} + V_{sf}^{b+1} \right)^{1/(b+1)}$$

$$\times \Theta(v_i - v_{frag}).$$ (15)

Substituting $c_1 = M(b+1)/(2a\mathcal{V}V_{agg}^{b+1})$ and $c_2 = ((b+1)(T_f + \chi)/a\mathcal{V} - V_{sf}^{b+1})/V_{agg}^{b+1}$, this simplifies to

$$\mu(v_i) = 1 - [c_1 v_i^2 - c_2]^{1/(b+1)} \Theta(v_i - v_{frag}),$$ (16)

where we set $b = -1.2$ according to the measured mass distribution and set the fragmentation threshold to $v_{frag} = 0.75$ m s^{-1} as determined from the measurements. Fitting this to our data results in $c_1 = (-0.073 \pm 0.027)$ s^2 m^{-2} and $c_2 = -1.49 \pm 0.1$, which gives our model function plotted in Figure 6.

For the limiting case $T_f + \chi \gg \mathcal{V}$, we furthermore get a proportionality of the ratio between the volume of the smallest fragment and the whole aggregate and the contact energy $\mathcal{V}$ to

$$\frac{V_{sf}}{V_{agg}} \propto \mathcal{V}^{-1/(b+1)}.$$ (17)

We note that other authors like Beitz et al. (2011) or Deckers & Teiser (2015) describe the fragmentation strength of (dust) aggregates by a simple power law. Certainly our data could also be fitted by a power law. However, there is no physical meaning in this power law but to provide an analytical equation and the spread of data for all cited data, and ours is so large that there is no clear discriminator between these functions. A striking difference is that due to the Heaviside function our model has a limited upper value for fragmentation strength somewhat below 1 if fragmentation occurs.

Krijt et al. (2013) used similar assumptions to derive the smallest size of the fragment, namely, a power-law size distribution, and the dissipation of energy by creating fragments though their approach is based on surface energy of the new particle surface created. If the smallest size would be fixed, e.g., due to monomers in an aggregate and the sticking energy would be size independent (s. factor $N\mathcal{V}$ from Equation (12)), this should result in the same fragmentation strength model.
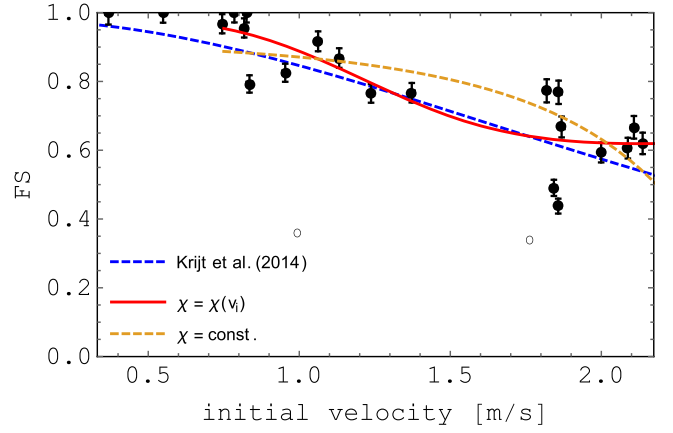

Figure 11. Comparison of fragmentation models for phononic and non-phononic dissipation. The circled data points were not used for the fit.

4.2. Extension of the Fragmentation Model

The simple fragmentation model has a cutoff in fragmentation strength somewhat below 1 at v_{frag}. We consider this sufficient for our data set and other data sets on first order (e.g., also Figure 10 in Deckers & Teiser 2014 shows a cutoff). However, it does not treat the transition. In this section, we therefore extend this model slightly. We consider the dissipation $\chi(v_i)$ to depend on the initial velocity v_i.

We mainly attribute the dissipation within the aggregate to phononic interaction. To approximate this interaction, we relate it to the harmonic oscillator so that the phonons can take the discrete energy levels $E_n = \hbar\omega(n + 1/2)$ only. Furthermore, the dispersion relation should be linear $\omega \propto p$ with the momentum p of the phonons. With these two assumptions, the momentum transfer Δp to phonons will only be possible at the multiple n of a discrete velocity v_R,

$$\Delta p(v_i) \propto \sum_n \delta(v_i - nv_R).$$ (18)

To describe the macroscopic body, we smooth the delta distributions $\delta(i_i - nv_R)$ with Gaussian curves

$$\sum_n \delta(v_i - nv_R) \longrightarrow \sum_n \exp(-(v_i - nv_R)^2)$$ (19)

and look at the limiting case $v_R \to 0$. This provides the dissipative term $\chi(v_i)$ as

$$\chi(v_i) \propto \lim_{v_R \to 0} \int_0^{v_i} \Delta p(v_i^*) dv_i^*$$

$$\propto \int_0^{v_i} \exp(-v_i^{*2}) dv_i^* \propto \mathrm{erf}(v_i)$$ (20)

or with a constant χ_0

$$\chi(v_i) = \chi_0 \mathrm{erf}(v_i).$$ (21)

For the fragmentation strength, this extension leads to

$$\mu(v_i) = 1 - [\zeta_1 v_i^2 - \zeta_2 \mathrm{erf}(v_i) - \zeta_3]^{1/(b+1)} \Theta(v_i - v_{frag})$$ (22)

with the constants $\zeta_1 = c_1 = M(b+1)/(2a\mathcal{V}V_{agg}^{b+1})$, $\zeta_2 = ((b+1)\chi_0/a\mathcal{V} - V_{sf}^{b+1})/V_{agg}^{b+1}$, and $\zeta_3 = ((b+1)T_f/a\mathcal{V} - V_{sf}^{b+1})/V_{agg}^{b+1}$. Figure 11 shows a comparison of the models for phononic and non-phononic dissipation.
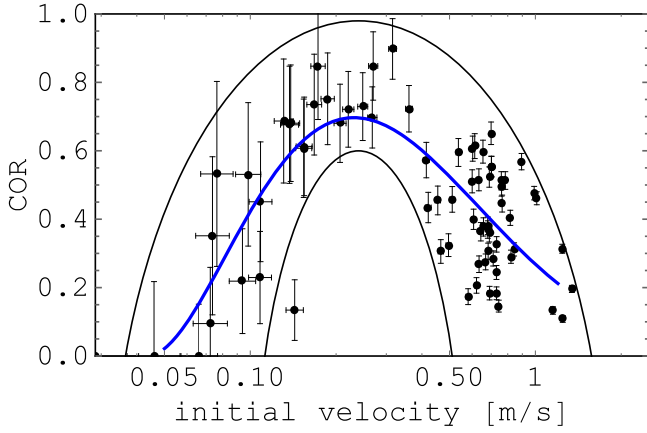
Figure 12. Coefficient of restitution on a logarithmic scale. An elliptical envelope is overplotted around the axis of symmetry.

For the constants from the fit, we get $\zeta_1 = 0.01 \pm 0.036 \, \text{s}^2 \, \text{m}^{-2}$, $\zeta_2 = (2.32 \pm 1.01)$, and $\zeta_3 = -3.5 \pm 0.9$. The benefit of the model with phononic dissipation is the behavior for $v_i \to 0$. Here, we get $\mu \to 1$ for $v_{\text{frag}} \to 0$. We note that this model is capable of handling the steep transitions in Deckers & Teiser (2014). It also agrees well with better resolved transition data (J. Deckers & J. Teiser 2016, private communication).

For a simple consideration of the fragmentation strength without smooth transitions at v_{frag}, the dependence on velocity can be neglected in the extended addend $\zeta_2 \, \text{erf}(v_i)$. As a result, the data can then be fitted with two parameters only, as shown in Figure 6.

4.3. Restitution Model

As a starting point, we take a look at the coefficient of restitution on a logarithmic scale, as Figure 12 shows. Overplotting an elliptical envelope centered at a velocity v_c suggests that the shape of the data implies the existence of a line symmetry as soon as we transform $v_i \to \tilde{v}_i = \ln(v_i/v_c)$. Forces, which are responsible for the cohesion, seem to have a similar nature to forces between contacts of grains, which have to be overcome for plastic deformation on a multiplicative scale.

The enclosing envelope $G_\epsilon(v_i)$ can be parameterized by

$$G_\epsilon(v_i) = \delta_1 + \sqrt{\delta_2 + \delta_3 \ln\left(\frac{v_i}{\delta_4}\right)^2} \qquad (23)$$

with $\delta_1 = -0.5$, $\delta_2 = 2.19$, $\delta_3 = -0.55$, $\delta_4 = 0.24 \, \text{ms}^{-1}$ for the upper boundary and $\delta_1 = -0.5$, $\delta_2 = 1.2$, $\delta_3 = -1.7$, $\delta_4 = 0.24 \, \text{ms}^{-1}$ for the lower boundary. δ_4 describes the critical velocity $v_c := \delta_4$.

Once this symmetry applies, the derivative $\epsilon'(\tilde{v}_i)$ has to be point symmetrical in $\tilde{v}_i$. Here, we approximate this by a linear symmetry $\epsilon'(\tilde{v}_i)/\epsilon(\tilde{v}_i) = a_1 \tilde{v}_i$ with a constant a_1. This might also be written as

$$\frac{\epsilon'(\tilde{v}_i)}{\epsilon(\tilde{v}_i)} = \frac{d}{d\tilde{v}_i} \ln(\epsilon(\tilde{v}_i)) = a_1 \tilde{v}_i. \qquad (24)$$

Integrating and solving for $\epsilon(\tilde{v}_i)$, this gives

$$\epsilon(\tilde{v}_i) = \exp(a_1 \tilde{v}_i^2 + a_2) \qquad (25)$$

with a second constant a_2. Now we can transform back to a term depending on v_i. This finally leads to

$$\epsilon(v_i) = A \cdot \exp\left(a_1 \left(\ln\left(\frac{v_i}{v_c}\right)\right)^2\right) \qquad (26)$$

with $A = \exp(a_2)$.

In the experiment we point out a sticking velocity v_{stick}, which Equation (26) does not consider so far. We can fulfill this condition with a linear transformation $v_i \to v_i - v_{\text{stick}}$ and multiplication by $\Theta(v_i - v_{\text{stick}})$, so that $\epsilon(v_i) = 0 \; \forall \; v_i < v_{\text{stick}}$. In total, we gain a function for the coefficient of restitution

$$\epsilon(v_i) = A \cdot \exp\left(a_1 \left(\ln\left(\frac{v_i - v_{\text{stick}}}{v_c}\right)\right)^2\right) \Theta(v_i - v_{\text{stick}}). \quad (27)$$

Strictly speaking, this transformation breaks the assumed symmetry to some extent. The coefficient of restitution decreases more in the neighborhood of the sticking velocity than for high velocities, which can be observed in Figure 12.

For our data, we get $A = 0.67 \pm 0.04$, $v_c = (0.189 \pm 0.025)$ m s^{-1}, $a_1 = -0.36 \pm 0.04$, and $v_{\text{stick}} = (0.04 \pm 0.02)$ m s^{-1}. The dependency in Equation (27) has a universal nature. For $v_{\text{stick}} = 0$, it gives the lognormal distribution, which is used widely, for example, in fitting distributions of particle sizes (Raabe 1971), describing the magnetization behavior of nm-Al particles (Buhrman & Granqvist 1976) or even biological systems (Koch 1966). For $a_1 = -1$ and $v_{\text{stick}} = 0$, we obtain the empirical equation from Higa et al. (1996, 1998), where

$$\epsilon(v_i) = A \cdot \left(\frac{v_i}{v_c}\right)^{-\ln\left(\frac{v_i}{v_c}\right)} = A \cdot \exp\left(-\left(\ln\left(\frac{v_i}{v_c}\right)\right)^2\right) \qquad (28)$$

was used to describe the collision behavior of centimeter-sized H_2O-ice spheres in the inelastic region.

5. CONSEQUENCES FOR PLANET AND COMET FORMATION

If grains outside the CO_2 ice line have onion-like shells, the outer CO_2 shell is thick enough to dominate the sticking properties. Certainly, fragmentation of shell-like bodies might be different (Geretshauser et al. 2011). However, for the low-energy collisions considered here, we regard the pure CO_2 collisions as a well-suited analog. We picture a possible simple result of our studies in Figure 1.

If no further recycling and phase transitions occur, there will be a torus of several AU (zone 2) between the water ice line and CO_2 ice line where planetesimals form preferentially. Farther in and farther out, growth will proceed slower or get stuck, e.g., at bouncing barriers before instabilities can kick in. Another possibility is that larger ice structures could form in upper (warmer) disk layers, where H_2O ice in contrast to CO_2 ice is still present. Those aggregates could cross the CO_2 snow line due to vertical settling resulting in sweep up of smaller CO_2 coated particles and finally runaway growth of a limited number of aggregates as, e.g., described for "lucky winners" in Windmark et al. (2012).

Other scenarios are possible as well. Gravitational instability, for example, can be partly sensitive to certain sizes. Therefore, it might be beneficial if growth does not proceed to large structures. In this case, zone 1 or zone 3 might be favored

for planetesimal formation. Also, in the vicinity of the ice lines and especially in turbulent disks phase transitions might be frequent with sublimation and recondensation changing the structure of the solids constantly. This might also be beneficial to form larger bodies (Ros & Johansen 2013). Nevertheless, CO_2 collisions would dominate the further evolution also in this picture at later times.

This shows some potential outcomes, which require more complex modeling, but put emphasize on the importance of CO_2 collisions. It is crucial to note that ices can behave very differently. We only consider CO_2 ice in this work but the concept of ice lines does not end here. CO was already mentioned above. How CO collisions proceed is unknown. Considering the dipole moment as a crucial factor for the collisional outcome, CO should behave similar to CO_2 ice since the dipole moment of CO of 0.112 D is very small compared to the dipole moment of H_2O of 1.84 D (Scuseria et al. 1991). There are also "high temperature" ice lines. Lodders (2004) e.g., propose the existence of a tar line inside of the water ice line to explain compositional details of Jupiter.

The similarity to silicate properties does not necessarily prevent formation of planetesimals in zone 3 as there are terrestrial planets supposed to be formed in zone 1. However, formation timescales and final size and composition of the forming objects (comet, planetesimal, or planet) might be different.

6. CONCLUSION

We measured the threshold impact speeds between sticking and bouncing and between bouncing and fragmentation of $\sim 100\,\mu m$ sized CO_2-ice aggregates. We obtain a sticking threshold of $v_{stick} = (0.04 \pm 0.02)\,\mathrm{m\,s^{-1}}$. Scaled in size, this is similar to silicates (Poppe et al. 2000) but a factor of 10 less than for water ice (Gundlach & Blum 2015). We derive a surface energy of $\gamma = 0.17^{+0.26}_{-0.13}\,\mathrm{J\,m^{-2}}$ for CO_2 ice. After the bouncing regime fragmentation sets in at $v_{frag} = (0.75 \pm 0.05)\,\mathrm{m\,s^{-1}}$. Critical fragmentation occurs at $v_{crit} = (2.19 \pm 0.05)\,\mathrm{m\,s^{-1}}$. The size distribution of fragments except the largest one follows a power law $n \propto m^{-1.2 \pm 0.1}$, consistent with aggregates of silicate grains (Güttler et al. 2010). The critical fragmentation energy is also comparable to the energy deduced from tensile strength measurements of $100\,\mu m$ basalt-, and palagonite aggregates (C. de Beule et al. 2015, in preparation). This all implies that CO_2 ice behaves like silicates in collisions.

We further developed a model for fragmentation (Equation (16)) and restitution (Equation (27)). Within this model, the fragmentation strength depends mainly on the size distribution of the fragments, which has to be known from empirical measurements. We obtain a similar equation for the coefficient of restitution as Higa et al. (1996, 1998) used for centimeter-sized H_2O-ice spheres.

To conclude, the term ice in planetesimal formation is often used with the tacit understanding that it is water ice. Water ice is more sticky due to the dipole interactions. It is tempting to assume that beyond the water snow line the stickiness increases for all kinds of particles and aggregates. As shown here, this is not the case. Collisions of (pure) CO_2 ice grains are much more comparable to the collisions of silicate grains. If CO_2 covers water-ice grains beyond 10 AU, collisions farther out will be less sticky then farther inward. This restricts a water-ice-dominated preferential planetesimal formation to a torous of a few AU between the water ice line and the CO_2 ice line.

REFERENCES

Ali-Dib, M., Mousis, O., Petit, J.-M., & Lunine, J. I. 2014, in SF2A-2014: Proc. Annual Meeting of the French Society of Astronomy and Astrophysics, ed. J. Ballet et al., 169
Andrews, J. 1930, The London, Edinburgh, and Dublin Philosophical Magazine and Journal of Science, 9, 593
Antonyuk, S., Heinrich, S., Tomas, J., et al. 2010, Granular Matter, 12, 15
Aumatell, G., & Wurm, G. 2011, MNRAS, 418, L1
Aumatell, G., & Wurm, G. 2014, MNRAS, 437, 690
Baruteau, C., Crida, A., Paardekooper, S., et al. 2013, arXiv:1312.4293
Beitz, E., Güttler, C., Blum, J., et al. 2011, ApJ, 736, 34
Blum, J., & Wurm, G. 2000, Icar, 143, 138
Blum, J., & Wurm, G. 2008, ARA&A, 46, 21
Borderies, N., Goldreich, P., & Tremaine, S. 1984, in IAU Colloq. 75, Planetary Rings, ed. R. Greenberg & A. Brahic (Toulouse: Obs. De Paris), 713
Bryson, C. E., Cazcarra, V., & Levenson, L. L. 1974, Journal of Chemical Engineering Data, 19, 107
Buhrman, R. A., & Granqvist, C. G. 1976, JAP, 47, 2220
Chiang, E., & Youdin, A. N. 2010, AREPS, 38, 493
Deckers, J., & Teiser, J. 2014, ApJ, 796, 99
Deckers, J., & Teiser, J. 2016, MNRAS, 456, 4328
Dittkrist, K.-M., Mordasini, C., Klahr, H., Alibert, Y., & Henning, T. 2014, A&A, 567, A121
Dittrich, K., Klahr, H., & Johansen, A. 2013, ApJ, 763, 117
Dominik, C., Blum, J., Cuzzi, J. N., & Wurm, G. 2007, Protostars and Planets V (Tuscon, AZ: Univ. of Arizona Press)
Dominik, C., & Tielens, A. G. G. M. 1997, ApJ, 480, 647
Fayolle, E. C., Öberg, K. I., Cuppen, H. M., Visser, R., & Linnartz, H. 2011, A&A, 529, A74
Geretshauser, R. J., Meru, F., Speith, R., & Kley, W. 2011, A&A, 531, A166
Gundlach, B., & Blum, J. 2015, ApJ, 798, 34
Güttler, C., Blum, J., Zsom, A., Ormel, C. W., & Dullemond, C. P. 2010, A&A, 513, A56
Hässig, M., Altwegg, K., Balsiger, H., et al. 2015, Sci, 347, 2761
Hayashi, C., Nakazawa, K., & Nakagawa, Y. 1985, in Protostars and Planets II, ed. D. C. Black, & M. S. Matthews
Helled, R., Bodenheimer, P., Podolak, M., et al. 2014, Protostars and Planets VI (Tuscon, AZ: Univ. of Arizona Press)
Higa, M., Arakawa, M., & Maeno, N. 1996, P&SS, 44, 917
Higa, M., Arakawa, M., & Maeno, N. 1998, Icar, 133, 310
Johansen, A., Blum, J., Tanaka, H., et al. 2014, Protostars and Planets VI (Tuscon, AZ: Univ. of Arizona Press)
Kataoka, A., Tanaka, H., Okuzumi, S., & Wada, K. 2013, A&A, 557, L4
Kelling, T., Wurm, G., & Köster, M. 2014, ApJ, 783, 111
Kley, W., & Nelson, R. P. 2012, ARA&A, 50, 211
Koch, A. L. 1966, Journal of Theoretical Biology, 12, 276
Krijt, S., Güttler, C., Heißelmann, D., Dominik, C., & Tielens, A. 2013, JPhD, 46, 435303
Krijt, S., & Kama, M. 2014, A&A, 566, L2
Lin, T.-C., Shen, Y.-J., & Wang, M.-R. 2014, AerST, 48, 228
Lodders, K. 2004, ApJ, 611, 587
Mazzoldi, A., Hill, T., & Colls, J. J. 2008, International Journal of Greenhouse Gas Control, 2, 210
Morrison, M. A., & Hay, P. J. 1979, JChPh, 70, 4034
Öberg, K. I., Murray-Clay, R., & Bergin, E. A. 2011, ApJL, 743, L16
Okuzumi, S., Tanaka, H., Kobayashi, H., & Wada, K. 2012, ApJ, 752, 106
Pollack, J. B., Hubickyj, O., Bodenheimer, P., et al. 1996, Icar, 124, 62
Pontoppidan, K., Salyk, C., Bergin, E., et al. 2014, Protostars and Planets VI (Tuscon, AZ: Univ. of Arizona Press)
Poppe, T., Blum, J., & Henning, T. 2000, ApJ, 533, 454
Qi, C., Öberg, K. I., Wilner, D. J., et al. 2013, Sci, 341, 630
Raabe, O. G. 1971, JAerS, 2, 289
Ros, K., & Johansen, A. 2013, A&A, 552, A137
Scuseria, G. E., Miller, M. D., Jensen, F., & Geertsen, J. 1991, JChPh, 94, 6660
Sirono, S. 2013, ApJ, 765, 50
Span, R., & Wagner, W. 1996, JPCRD, 25, 1509
Teiser, J., Engelhardt, I., & Wurm, G. 2011, ApJ, 742, 5
Teiser, J., & Wurm, G. 2009, MNRAS, 393, 1584
Thornton, C., & Ning, Z. 1998, Powder Technology, 99, 154
Wada, K., Tanaka, H., Suyama, T., Kimura, H., & Yamamoto, T. 2009, ApJ, 702, 1490

Wettlaufer, J. 2010, ApJ, 719, 540
Windmark, F., Birnstiel, T., Güttler, C., et al. 2012, A&A, 540, A73
Wood, S. E. 1999, PhD thesis, Univ. of California
Wurm, G., Blum, J., & Colwell, J. E. 2001, PhRvE, 64, 046301

Wurm, G., Paraskov, G., & Krauss, O. 2005, Icar, 178, 253
Yamashita, Y., & Kato, M. 1997, GeoRL, 24, 1327
Zsom, A., Ormel, C. W., Güttler, C., Blum, J., & Dullemond, C. P. 2010, A&A, 513, A57